ACIN

Controlling the Amplitude of a Resonant Rotational Reluctance Actuated Scanning Mirror System

D. Pechgraber* E. Csencsics* H. Yoo* G. Schitter*

*Automation and Control Institute TU Wien, 1040 Vienna, Austria,
(Corresponding author e-mail: pechgraber@acin.tuwien.ac.at).*

Abstract: This paper describes the development and implementation of three driving strategies for the oscillation amplitude control of a resonant rotational reluctance actuated scanning mirror system. The three driving strategies exploit control of current input amplitude, pulse duration, and the phase between the input and the mover angle. Linear PI-controllers are developed for each driving strategy for the linearized plant around an operating point of the highly nonlinear system. The implemented driving strategies are compared over a wide operating range of the scanning mirror system, regarding their closed-loop dynamics in the time-domain, revealing their fundamental differences. Phase-control is the most promising control strategy, delivering the highest closed-loop bandwidth of at least 11 Hz over the entire investigated operating range at worst with a rise-time of 30 ms at a step response.

Keywords: Mechatronics, Control, Reluctance Actuator, Scanning Mirror System

1. INTRODUCTION

Scanning mirror systems are devices, which reflect an incoming light beam and change its direction in a proper way. They are used in various different applications including systems for confocal microscopy [Ji et al. (2008)], scanning optical lithography [Zhou et al. (2008)], optical coherence topography [Gorecki and Bargiel (2020)], light detection and ranging (LiDAR)[Yoo et al. (2022)], SLA 3D-printing [Huang et al. (2020)], and micro-machining [Loor (2013)].

For scanning applications resonant scanning mirror systems are commonly used, which are driven at the resonance frequency of their mechanical structure, in order to reach high scanning amplitudes [Wang et al. (2020)]. Higher scanning amplitudes increase the optical field of view of the reflected laser beam. The reflecting mirror aperture is usually only in the order of a few millimeters for very fast systems with a scanning frequency of greater than 2 kHz [Senger et al. (2020); Hofmann et al. (2012)]. However, for some applications larger aperture sizes are desirable because of the required waist of the reflected laser beam, such as SLA 3D-printing [Quan et al. (2020)] or micro-machining [Loor (2013)]. Beam diameters of 6 mm and more are commonly used in these applications [Loor (2013)]. For these applications usually fast steering mirror (FSM) systems are used, which are commonly actuated by Lorentz-force based voice-coil actuators for larger scan range, piezo-electric actuators for higher bandwidth [Csencsics et al. (2018)], or by reluctance force which relaxes the trade-off between scanning range and bandwidth [Csencsics and Schitter (2021)]. Recently scanning systems integrating the reluctance actuation principle have been proposed [Csencsics et al. (2018); Li et al. (2017)].

The reluctance actuated systems have in common that the driving coils are located beneath the mover, which limits the scanning range to the air gap length. This requires a trade-off between achievable reluctance force, which is higher for shorter air-gaps, and achievable scanning range [Csencsics and Schitter (2021)]. To circumvent the mechanical limitation, a large aperture resonant rotational reluctance actuator was developed, in which the ferromagnetic yoke is placed at the side of the mover [Pechgraber et al. (2023)]. It achieves a mechanical scanning range of ± 13.5 deg.

Similar to the resonant reluctance actuator, resonant comb-actuated micro-electro-mechanical system mirrors (MEMS-mirrors) also rely solely on attractive forces due to their actuation principle. For the control of these MEMS-mirrors the variation of the input amplitude, the duty-cycle of the actuation pulses and the phase between the actuation and the mover angle are reported. Combinations of duty-cycle and phase-control [Maksymova et al. (2019); Yoo et al. (2022)], and a combination of amplitude and phase-control [Brunner et al. (2021a)] are applied. A novel linear modeling approach of the local dynamics of resonant micro-mirrors based on energy-conservation is presented in [Brunner et al. (2021b)]. It is shown, that a linear PI-controller in combination with a phase locked loop (PLL) is applicable for the oscillation amplitude control over a wide amplitude range. However, as this system is actuated by electro-static driven comb-drives its behaviour is different from the resonant reluctance actuation principle.

The contribution of this paper is the development of three driving strategies for the oscillation amplitude control of a resonant rotational reluctance actuated scanning mirror system, and their evaluation on an experimental prototype setup. After the working principle and experimental
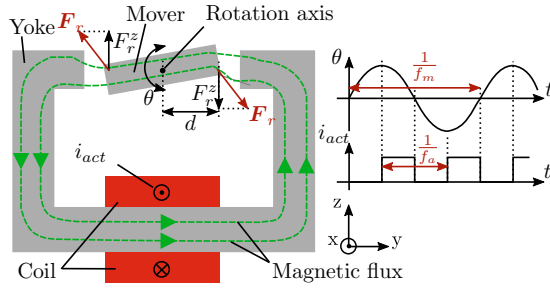
ACIN

Fig. 1. Resonant rotational reluctance actuator working principle: The magnetic flux generated by the current in the actuator coil i_{act} is guided to the mover via a ferromagnetic yoke. The current is controlled in a way, that the reluctance force upholds an oscillating motion of the mover around its rotation axis.

prototype system is introduced in Section 2, three driving strategies are derived in Section 3 to vary the injected energy into the systems mover oscillation, allowing to control the scanning amplitude. In Section 4 transfer functions for the linearized system are identified in different operating points, followed by the design of tailored controllers for each driving strategy. The corresponding closed-loop dynamics are evaluated over a wide operating range in Section 5 whereupon the paper is concluded in Section 6.

2. SYSTEM DESCRIPTION

2.1 Resonant Rotational Reluctance Actuation Principle

Figure 1 shows the working principle of the resonant rotational reluctance actuator [Pechgraber et al. (2023)]. A ferromagnetic mover is suspended by a flexure structure, which enables the rotation around its rotation axis (parallel to x-axis) and restricts the other degrees of freedom (DoF). For generating a scanning motion of the mover, it is actuated by the reluctance force between the ends of the ferromagnetic yoke and the mover. In the presence of a magnetic flux (green dashed lines), the reluctance force $\boldsymbol{F}_r$ acts on the mover. The force components in z-direction F_r^z result in a net torque around the rotational axis if the mover is deflected from its equilibrium position by an angle $|\theta| > 0$.

The reluctance force is proportional to the square of the coil current i_{act}, and thus a solely attractive force [Schmidt et al. (2020)]. Hence, only pulling forces can be applied to the mover in this configuration. Such systems are usually driven by a square-wave signal with twice the oscillating frequency of the mover, which is called first-order parametric resonance [Frangi et al. (2017)]. This means that the actuator coil current is driven with the frequency f_a, which is twice the mover frequency f_m. In Fig. 1 the case is shown, in which the current is switched on exactly at the peak of the mover oscillation and switched off in the equilibrium position, avoiding a deceleration of the mover, which is called synchronized excitation [Brunner et al. (2021a); Schenk et al. (2000)].

As a consequence of the operation in first-order parametric resonance, instability occurs at the movers equilibrium
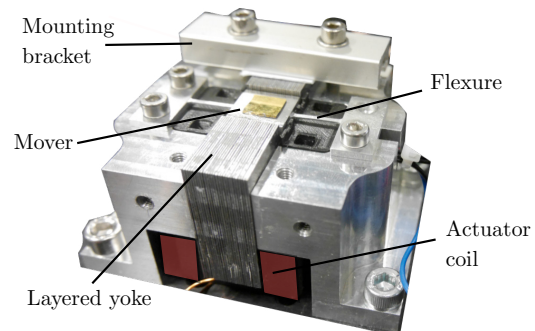

Fig. 2. Partly assembled actuator prototype with a layered yoke, which is held in place by mounting brackets. Further, the mover suspended by a torsional beam flexure can be seen with a mirror attached on the top.

position $\theta = 0$ [Champneys (2009)]. For this reason, already small perturbations from the equilibrium position, like vibrations or an initial offset by mounting tolerances lead to the start of the mover oscillation. Therefore, the automatic startup of the system is possible by simply applying the mentioned actuation signal to the actuator.

2.2 1DoF Scanning System Prototype

The experimental evaluation of the different driving strategies of the resonant rotational reluctance actuator are carried out on a 1DoF scanning mirror prototype system [Pechgraber et al. (2023)]. The partly assembled prototype system is shown in Fig. 2. On the top, the ferromagnetic mover is visible, which is suspended via a torsional beam flexure. This torsional beam flexure enables the desired rotational movement at a mechanical resonance frequency of 223 Hz, while suppressing the other DoFs [Pechgraber et al. (2023)]. The angular position of the mover is measured by two optical proximity sensors beneath the mover. A layered ferromagnetic yoke guides the magnetic flux generated by the actuator coil to the mover. Layering of the yoke reduces the unwanted phase-loss between magnetic flux and current and ohmic losses in the yoke, which are caused by eddy-currents [Csencsics et al. (2017)]. The actuator coil is driven by a custom made full-bridge pulse generator, generating the required voltage pulses for magnetizing and demagnetizing the actuator coil. A dSpace system (MicroLabBox, dSPACE GmbH, Germany) is used for the implementation of the switching logic that drives the pulse generator and for the control strategies presented in this paper.

3. DRIVING STRATEGIES

As can be seen in Fig. 1, the reluctance force generated by the actuator coil is used for upholding the oscillation of the mover. The reluctance torque acting on the mover can be approximated by [Pechgraber et al. (2023)]

$$\tau(\theta, i_{act}) = -c_1\theta(t)i_{act}^2(t) \tag{1}$$

with the current in the actuator coil $i_{act}(t)$, the mover deflection angle from the equilibrium position $\theta(t)$ and a positive fitted constant c_1. By integrating the torque over
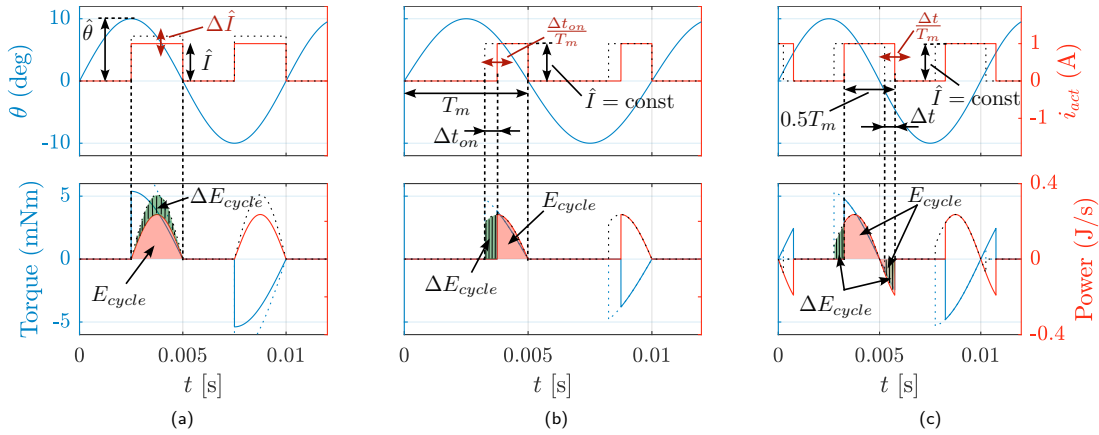
Fig. 3. Three actuator coil driving strategies for the variation of the injected energy into the system. The mover deflection angle θ with idealized actuator coil current i_{act} and the respective mover torque is shown in the case of $\hat{I}$-control (a), t_{on}-control (b) and phase-control (c). The area under the power curves can be interpreted as the injected energy per actuation cycle (E_{cycle}).

the traveled angle θ the energy injected into the system in one actuation cycle can then be calculated by [Brunner et al. (2021b)]

$$E_{cycle} = \int_{\theta(0)}^{\theta(T_m)} \tau(\theta, i_{act}) d\theta$$

$$= \int_{\theta(0)}^{\theta(T_m)} -\left(c_1 \theta(t) i_{act}^2(t)\right) d\theta . \qquad (2)$$

In steady state operation for a constant ocillation amplitude the injected energy has to compensate the energy that is dissipated via damping in this period of time. In order to further control the oscillation amplitude of the system, E_{cycle} has to be varied by a controller. Figure 3 shows the three driving strategies, enabling the manipulation of the injected energy. These are the variation of either the input current amplitude, the actuation pulse duration, or the phase between the input and the mover angle. The plots show the mover deflection angle θ with idealized actuator coil currents i_{act} and the respective torque on the mover according to (1). The integration variable in (2) is the mover angle θ, and not the time t. To better understand the way the energy is injected into the system, the injected power over time is additionally plotted.

The first driving strategy in Fig. 3a shows the variation of the current pulse amplitude $\hat{I}$, referred to as $\hat{I}$-control. In this case, the actuator coil is switched on exactly at the peak of the mover osillation $\hat{\theta}$ and turned off at the zero-crossing. By assuming ideal rectangular shaped actuator current pulses, (2) can be evaluated to

$$E_{cycle}^{\hat{I}} \approx \int_{\hat{\theta}}^{0} -\left(c_1 \theta \hat{I}^2\right) d\theta = \frac{1}{2} c_1 \hat{\theta}^2 \hat{I}^2 , \qquad (3)$$

in the case of $\hat{I}$-control. This energy can be interpreted as the area below the power curve in Fig. 3a (red area). If the

current amplitude is changed by $\Delta\hat{I}$, a change of injected energy per actuation cycle ΔE_{cycle} is the consequence (green shaded area).

The second driving strategy is the variation of the current pulse duration, i.e. duty-cycle, while leaving the current amplitude $\hat{I}$ constant. In Fig. 3b the off time is fixed at the zero-crossing and the on time is varied. For the control implementation in the next section the on time is normalized to the actuation period time T_m, which is a half mover oscillation period. Therefore, the respective control variable is $\frac{t_{on}}{T_m}$. The injected energy can be expressed with the control variable, by evaluating (2) according to Fig. 3b, yielding

$$E_{cycle}^{t_{on}} \approx \int_{\theta(t_{on})}^{0} -\left(c_1 \theta \hat{I}^2\right) d\theta = \frac{1}{2} c_1 \hat{I}^2 \theta^2(t_{on}) . \qquad (4)$$

If a sinusoidal motion $\theta(t) = \hat{\theta} \sin(\omega_s t)$ with the angular frequency $\omega_s = \frac{\pi}{T_m}$ is assumed, the injected energy can be expressed by

$$E_{cycle}^{t_{on}} \approx \frac{1}{2} c_1 \hat{I}^2 \hat{\theta}^2 \sin^2\left(\pi \frac{t_{on}}{T_m}\right), \qquad (5)$$

for $\frac{t_{on}}{T_m} \in [0,1]$. As in the $\hat{I}$-control case the area under the power curve in Fig. 3b (red area) is the energy per actuation cycle E_{cycle}, and the energy difference ΔE_{cycle} (green shaded area) results from the change of the on time $\frac{\Delta t_{on}}{T_m}$. For the control implementation the sign of the control variable has to be inverted, because in the range $\frac{t_{on}}{T_m} \in [0.5,1]$ the injected energy function (5) has a negative slope. The system could also be driven in the range $\frac{t_{on}}{T_m} \in [0,0.5]$, but that causes losses by deceleration of the mover in the region before the amplitude.

Figure 3c shows the third case, in which the pulse duration and the current amplitude are constant, but the relative phase between the current pulse and the mover oscillation is varied. The introduced time shift Δt is again normalized

to the actuation period T_m for the control implementation, hence the control variable is $\frac{\Delta t}{T_m}$. With a sinusoidal motion, trigonometric identities and by neglecting variations of T_m and $\hat{\theta}$, the evaluation of (2) leads to

$$
\begin{aligned}
E_{cycle}^{\Delta t} &\approx \int_{\theta\left(\frac{T_m}{2}+\Delta t\right)}^{\theta(T_m+\Delta t)} -\left(c_1 \theta \hat{I}^2\right) d\theta \\
&= \frac{1}{2} c_1 \hat{I}^2 \hat{\theta}^2 \left[\sin^2\left(\frac{\pi}{2}+\frac{\Delta t}{T_m}\pi\right) - \sin^2\left(\pi + \frac{\Delta t}{T_m}\pi\right)\right] \\
&= \frac{1}{2} c_1 \hat{I}^2 \hat{\theta}^2 \cos\left(2\pi\frac{\Delta t}{T_m}\right),
\end{aligned}
\tag{6}
$$

for $\frac{\Delta t}{T_m} \in [0,1]$. In comparison to the other two driving strategies, the injected energy in an actuation cycle can get negative in the admissible range, so energy can also be withdrawn from the system. For the implementation the sign of the control variable has to be inverted again, because in the targeted driving range $\frac{\Delta t}{T_m} \in [0, 0.5]$ the injected energy function has a negative slope.

4. SYSTEM IDENTIFICATION AND CONTROL DESIGN

Because the system is nonlinear as can be seen in the derived functions for the injected energy in the previous section, linear control design procedures can only be applied for the linearized system around an operating point [Brunner et al. (2021b)]. For this reason, this section deals with the system identification for each driving strategy in different operating points and the control design.

4.1 System Identification

To enable the identification at specific oscillation amplitude setpoints $\hat{\theta}^d$, the identification is done in a closed-loop configuration. In Fig. 4 a block-diagram of the entire control system is shown. It consists of the actuator itself, the custom-made pulse generator for driving the actuator coil, sensor electronics, and the software parts implemented in the rapid prototyping system. The switching logic is responsible for the correct timing and amplitude of the actuator coil pulses, in dependence of the zero-crossings of the sensed mover angle θ and according to the control input of the respective driving strategy. The switching logic together with the zero-crossing detection acts as a phase locked loop (PLL).

For the identification a PI-controller is used, whose parameters are empirically tuned to obtain a stable oscillation amplitude at the desired setpoint $\hat{\theta}^d$. To detect the amplitude of the mover oscillation $\hat{\theta}$, the sensed mover angle is filtered with a 6th order Chebyshev low-pass filter with a cut-off frequency of $600\,\text{Hz}$. This reduces the remaining noise on the measured signal and ensures a correct detection of the amplitude values. The filter also adds a dead-time of $\approx 775\mu s$ at the scanning frequency of $223\,\text{Hz}$. However, a new amplitude value is gathered only once every mover oscillation period of 4.5ms, so the added dead-time is acceptable. For the system identification a network analyzer (Analog Discovery 2, Digilent, USA) is connected to the system according to Fig. 4. The sampling

time of the software system is $T_s = 25\,\mu s$, therefore the delay introduced by the analog-digital converters (ADCs) and digital-analog converters (DACs) of the system can be neglected and the plant transfer function $G(s)$ can be approximated with the measured signals by

$$
G(s) = \frac{\hat{\theta}(s)}{u(s)} \approx \frac{\gamma(s)}{\xi(s)},
\tag{7}
$$

with $u(s) \in \left\{\hat{I}(s), \frac{t_{on}}{T_m}(s), \frac{\Delta t}{T_m}(s)\right\}$. $\gamma(s)$ and $\xi(s)$ represent analog signals after the DACs of $\hat{\theta}$ and u respectively.

In Fig. 5 the result of the system identification is shown. For each driving strategy (blue, green, black) three amplitude set points ($2\,\text{deg}$, $5\,\text{deg}$, $8\,\text{deg}$) are investigated, marked with dotted, dashed and solid lines in the plot. In t_{on}-control and phase-control the injected energy functions (5) and (6) have a negative slope in the area of operation and thus the phase is inverted compared to $\hat{I}$-control. However, as the sign of the control variable is inverted in the implementation, the phase in these cases is shifted by $-180\,\text{deg}$ in Fig. 5.

The system shows 1st order low-pass behaviour with additional dead-time. For the set point $\hat{\theta}^d = 2\,\text{deg}$ the phase is $-90\,\text{deg}$ also for very low frequencies of below $1\,\text{Hz}$, what would suggest a pure integrator. However, if the integral gain of the implemented controller is turned off, a steady-state control error occurs, ruling out pure integral behaviour of the system. The phase-drop in all cases is mainly dominated by the dead-time introduced by the fact, that a new amplitude value is detected only once every oscillation cycle in the amplitude detection block of Fig. 4. The fitted dead-time in the phase-plot of Fig. 5 (red dashed line) corresponds to $T_{dt} = \frac{1}{223\text{Hz}} = 4.5\,\text{ms}$. The largest magnitude difference between the lowest and highest operating point is visible in $\hat{I}$-control.

4.2 Control Design

To design a robust controller for each driving strategy, the identified plant transfer functions $G(s)$ with the largest setpoint are used. Otherwise the open-loop cross-over frequency would be shifted to the right for higher operating points, reducing the respective phase-margin or even leading to an unstable system. By using the fitted dead-time from Fig. 5 and linear fits for the $-20\,\text{dB}$ slopes in Fig. 5 for each of the three driving strategies a PI-controller with the structure

$$
G_{PI}(s) = k\frac{1+sT}{s}
\tag{8}
$$

is designed. The phase-lag of the identified dynamics are given by

$$
\arg\left(G(j\omega)\right) = -\frac{\pi}{2} + \arg\left(e^{-sT_{dt}}\right) = -\frac{\pi}{2} - \omega T_{dt}.
\tag{9}
$$

If zero phase-lag from the controller is assumed, the maximum open-loop cross-over frequency for a desired phase-margin of $\Phi = 60\,\text{deg}$ can then be calculated by

$$
\omega_c = \frac{\frac{\pi}{2} - \Phi}{T_{dt}} = 115.18\,\text{rad/s} \equiv 18.3\,\text{Hz}.
\tag{10}
$$

The zero of the PI-controller (8) is placed a factor 10 below this frequency to justify the assumption of zero phase-lag at the cross-over frequency, so $T = \frac{10}{\omega_c}$. Afterwards
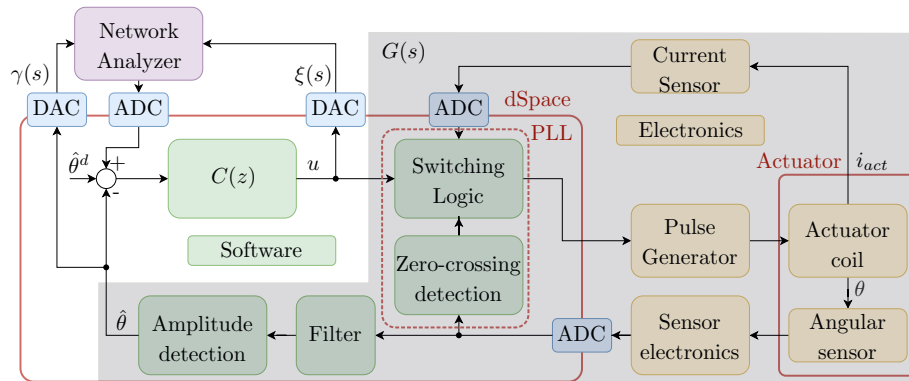
Fig. 4. Block diagram of the experimental prototype system. The actuator is driven by a custom made pulse generator which is controlled by the switching logic implemented in the dSpace system. For analyzing the plant in different operating points, a network analyzer is connected to DACs and an ADC of the dSpace system enabling closed-loop system identification.
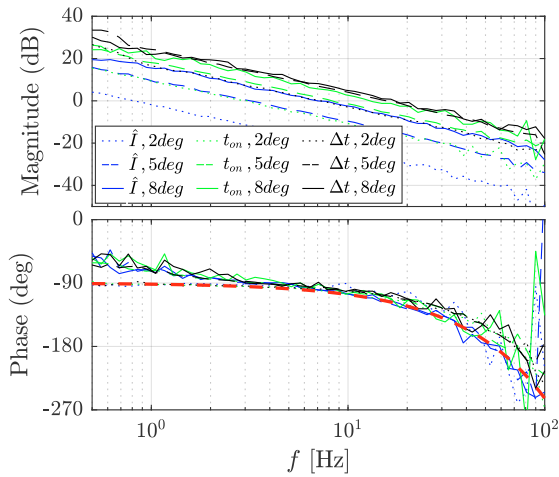

Fig. 5. Results of the system identification showing the plant transfer function for each driving strategy in 3 different operating points $\hat{\theta}^d$. The fitted time-delay $T_{dt} = 4.5\,\text{ms}$ is illustrated by the red dashed line in the phase plot.
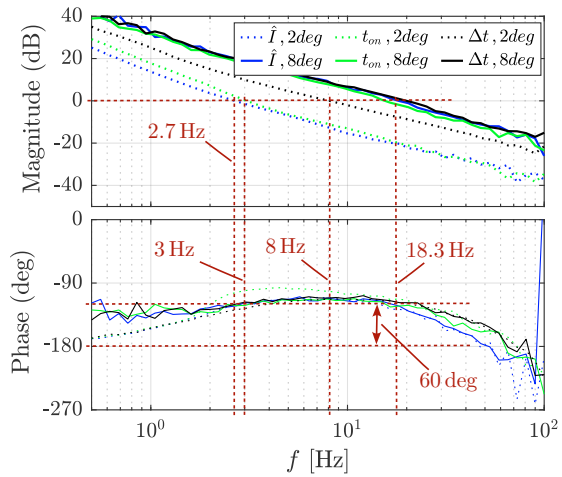
Fig. 6. Open-loop transfer functions with implemented PI-controller for each driving strategy. The controller are designed for the highest operating point ($\hat{\theta} = 8\,\text{deg}$), therefore the open-loop crossover frequency changes significantly for the lower operating point ($\hat{\theta} = 2\,\text{deg}$).

Table 1. Coefficients for the implemented PI-controller

Strategy	k	T	$\frac{\omega_c}{2\pi}$	Unit
$\hat{I}$-control	29.829	0.0868	18.3Hz	A/deg
t_{on}-control	15.0499	0.0868	18.3Hz	1/deg
phase-control	11.3962	0.0868	18.3Hz	1/deg

k is adjusted, so that the loop gain crosses the 0 dB line at the desired frequency. The given phase-margin results in the controller parameters from Table 1. For clarification also the units of the controller gains are given. The controller outputs are subject to certain physical limits, like $\hat{I} = 0\,\text{A}$ as lower bound for $\hat{I}$-control and $\frac{t_{on}}{T_m} \in [0.5, 1]$ or $\frac{\Delta t}{T_m} \in [0, 0.5]$ as bounds for t_{on}-control and

phase-control. Therefore the outputs are limited to their bounds by software and an algorithm is implemented to avoid integral wind-up.

For verification of the control design, the open-loop transfer functions with the designed PI-controllers are measured and are shown in Fig. 6. In the operating point $\hat{\theta}^d = 8\,\text{deg}$ the open-loop transfer function of all three driving strategies matches well with the expected cross-over frequency. Also the phase-margin is well in the targeted area of $\Phi = 60\,\text{deg}$. However, a large shift to lower cross-over frequencies is visible for the operating points with smaller amplitude. Especially for $\hat{I}$-control and t_{on}-control the cross-over frequency is reduced by a factor of 6.8 and 6 respectively, whereas for phase-control it is
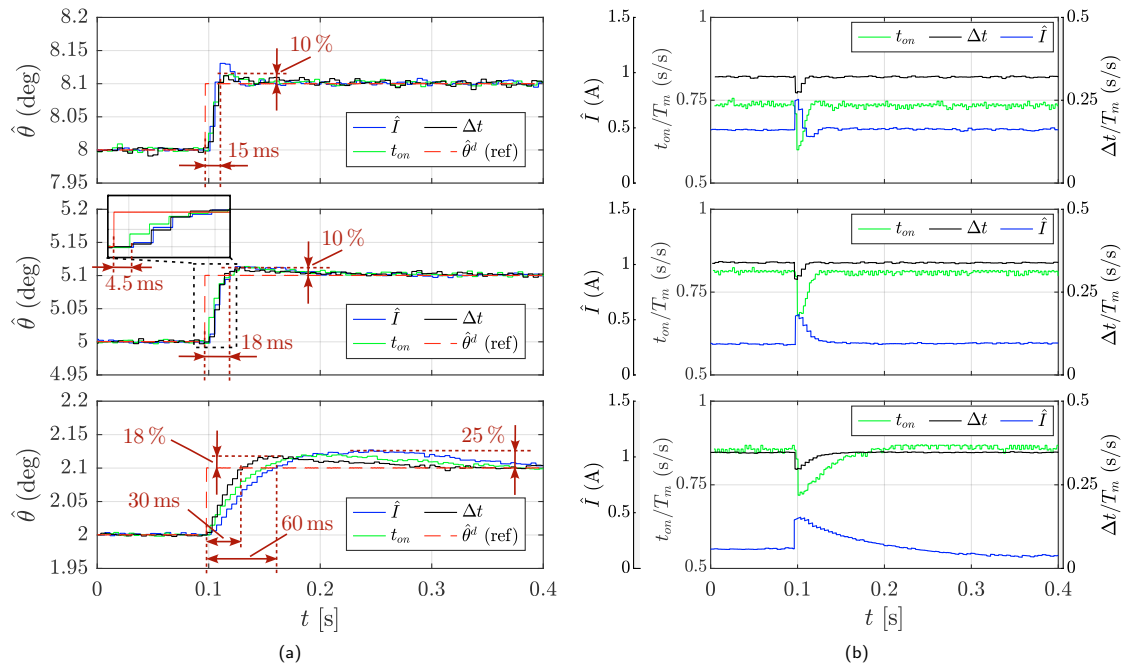
Fig. 7. Dynamic evaluation of the control system for each driving strategy by a step-response on the reference input. On the left the oscillation amplitude is shown together with the step on the reference input (a), and on the right side the corresponding control action is plotted (b).

only a factor of 2.3. Closed-loop measurements for the operating point $\hat{\theta}^d = 8$ deg reveal a closed-loop bandwidth of 29 Hz for $\hat{I}$-control and phase-control and 22 Hz for t_{on}-control (data not shown). In the lowest operating point $\hat{\theta}^d = 2$ deg phase-control has a closed-loop bandwidth of 11 Hz, whereas the other two driving strategies only have ≈ 3.5 Hz.

5. EXPERIMENTAL RESULTS

To evaluate how the different driving strategies affect the closed-loop dynamics of the system in the time-domain, a comparison of responses to reference input steps is performed. As in the open-loop transfer functions from Fig. 6, the same controller which is designed for the operating point $\hat{\theta}^d = 8$ deg is applied for every operating point, to enable a fair comparison between the driving strategies.

Figure 7 shows a step-response with 0.1 deg amplitude in each of the identified operating points. On the left side the oscillation amplitude is plotted together with the step on the reference input and on the right side the corresponding control action is shown for each driving strategy. For $\hat{\theta}^d = 8$ deg the dynamic performance is very similar for all driving strategies, because the controllers are tailored for this operating point. They show a rise-time of approximately 15 ms, with an overshoot of ≈ 10 %. The performance does not change much for $\hat{\theta}^d = 5$ deg with a rise-time of 18 ms and similar overshoot. In the zoomed

area of the middle plot, the delay of ≈ 4.5 ms brought into the system by the amplitude detection can be seen.

As expected from the measured open-loop transfer functions in Fig. 6, the biggest difference between the driving strategies is visible in the lowest operating point $\hat{\theta}^d = 2$ deg. In this case, the difference between phase-control and the other strategies is clearly visible. $\hat{I}$-control delivers with 60 ms a factor 2 higher rise-time than phase-control, and a 7 % higher overshoot. t_{on}-control shows a rise-time of 50 ms, which is a factor 1.7 higher as compared to phase-control, with comparable overshoot. The reason is the larger magnitude variation of the plant transfer function and the resulting lower open-loop cross-over frequency for the lower operating points for $\hat{I}$-control and t_{on}-control.

In summary, three different driving strategies for the oscillation amplitude control of a resonant rotational reluctance actuated scanning mirror system are developed and successfully demonstrated on an experimental prototype system. By varying either the current input amplitude, the pulse duration or the phase between actuation pulse and mover angle the amplitude of the scanning mirror system can be successfully controlled, whereby phase-control shows the smallest degradation of closed-loop dynamics for smaller operating points and outperforms the other driving strategies by at least a factor of 1.7 in rise-time during a step-response.

6. CONCLUSION

In this paper three different driving strategies for the oscillation amplitude control of a resonant rotational reluctance actuated scanning mirror system are designed and implemented on an experimental prototype system. Formulas for the injected energy into the system per actuation cycle are derived for each driving strategy based on idealized actuator signals. Due to the non-linear nature of the controlled system, PI-controllers are designed for the linearized plant around an operating point for each of the driving strategies and compared regarding their closed-loop dynamics. For three amplitude choices covering a wide operating range, phase-control shows a rise-time of $30\,\text{ms}$ to a step on the reference input at worst. This outperforms $\hat{I}$-control by a factor of 2 and t_{on}-control by a factor of 1.7. Phase-control with a linear PI-controller is therefore the most promising control strategy for the oscillation amplitude control of the resonant rotational reluctance actuated scanning mirror system in terms of a wide range of uniform operation.

REFERENCES

Brunner, D., Albert, S., Hennecke, M., Darrer, F., and Schitter, G. (2021a). Self-sensing control of resonant MEMS scanner by comb-drive current feedback. *Mechatronics*, 78, 102631.

Brunner, D., Yoo, H.W., and Schitter, G. (2021b). Linear Modeling and Control of Comb-Actuated Resonant MEMS Mirror With Nonlinear Dynamics. *IEEE Trans. Ind. Electron.*, 68, 3315–3323.

Champneys, A. (2009). Dynamics of parametric excitation. In *Encyclopedia of Complexity and Systems Science*, 2323–2345. Springer New York.

Csencsics, E. and Schitter, G. (2021). Exploring the Pareto Fronts of Actuation Technologies for High Performance Mechatronic Systems. *TMECH*, 26, 1053–1063.

Csencsics, E., Schlarp, J., and Schitter, G. (2017). Bandwidth extension of hybrid-reluctance-force-based tip/tilt system by reduction of eddy currents. In *AIM*, 1167–1172.

Csencsics, E., Schlarp, J., and Schitter, G. (2018). High-Performance Hybrid-Reluctance-Force-Based Tip/Tilt System: Design, Control, and Evaluation. *TMECH*, 23, 2494–2502.

Frangi, A., Guerrieri, A., Carminati, R., and Mendicino, G. (2017). Parametric resonance in electrostatically actuated micromirrors. *IEEE Trans. Ind. Electron.*, 64, 1544–1551.

Gorecki, C. and Bargiel, S. (2020). MEMS Scanning Mirrors for Optical Coherence Tomography. *Photonics*, 8, 6.

Hofmann, U., Janes, J., and Quenzer, H.J. (2012). High-Q MEMS Resonators for Laser Beam Scanning Displays. *Micromachines*, 3, 509–528.

Huang, J., Qin, Q., and Wang, J. (2020). A Review of Stereolithography: Processes and Systems. *Processes*, 8, 1138.

Ji, N., Shroff, H., Zhong, H., and Betzig, E. (2008). Advances in the speed and resolution of light microscopy. *Curr. Opin. Neurobiol.*, 18(6), 605–616.

Li, F., Zhou, P., Wang, T., He, J., Yu, H., and Shen, W. (2017). A Large-Size MEMS Scanning Mirror for Speckle Reduction Application. *Micromachines*, 8, 140.

Loor, R.D. (2013). Polygon scanner system for ultra short pulsed laser micro-machining applications. *Phys. Procedia*, 41, 544–551.

Maksymova, I., Greiner, P., Wiesmeier, J., Darrer, F., and Druml, N. (2019). A MEMS mirror driver ASIC for beam-steering in scanning MEMS-based LiDAR. In *Laser Beam Shaping XIX*, volume 11107, 64 – 71. SPIE.

Pechgraber, D., Csencsics, E., and Schitter, G. (2023). Resonant Rotational Reluctance Actuator for Large Range Scanning Mirrors. *TMECH*. (in press).

Quan, H., Zhang, T., Xu, H., Luo, S., Nie, J., and Zhu, X. (2020). Photo-curing 3d printing technique and its challenges. *Bioact. Mater.*, 5, 110–115.

Schenk, H., Durr, P., Haase, T., Kunze, D., Sobe, U., Lakner, H., and Kuck, H. (2000). Large deflection micromechanical scanning mirrors for linear scans and pattern generation. *IEEE J. Sel. Top. Quantum Electron.*, 6, 715–722.

Schmidt, R.M., Schitter, G., and Rankers, A. (2020). *The Design of High Performance Mechatronics - 3rd Revised Edition*. IOS Press.

Senger, F., Albers, J., Hofmann, U., Piechotta, G., Giese, T., Heinrich, F., Wantoch, T.v., and Gu-Stoppel, S. (2020). A bi-axial vacuum-packaged piezoelectric MEMS mirror for smart headlights. In *MOEMS and Miniaturized Systems XIX*, volume 11293, 27–33.

Wang, D., Watkins, C., and Xie, H. (2020). MEMS Mirrors for LiDAR: A Review. *Micromachines*, 11, 456.

Yoo, H.W., Brunner, D., Macho, M., Niedermueller, L., Devesa, A.J., Kormann, L., and Schitter, G. (2022). Evaluation of robustness against external vibrations for long-range MEMS lidar with one-dimensional resonant micromirror. *JOM*, 2.

Zhou, Q., Ben-Tzvi, P., Fan, D., and Goldenberg, A.A. (2008). Design of Fast Steering Mirror systems for precision laser beams steering. In *ROSE*, 144–149.